Direct-current piezoelectric energy harvesting based on plasmon-enhanced solar radiation pressure

Ha Young Lee[1], Min Sub Kwak[2], Geon-Tae Hwang[3], Hyung Soo Ahn[2], Robert A. Taylor[4], Dong Han Ha[5*] & Sam Nyung Yi[1,2*]

Abstract

A piezoelectric energy generating device that produces electricity using plasmon-enhanced solar radiation pressure (SRP) is developed. The SRP is greatly enhanced on the operational region of the device with a unique craterlike structure, and direct current is generated successfully on the device. By optimizing the material and thickness of top electrode, a maximum power density of 396 μW cm^{-2} is obtained. In addition, by using Raman measurements, finite-difference time-domain simulation, and COMSOL Multiphysics analysis, it is confirmed that the SRP is greatly amplified on the operational region with the nanoscale surface roughness due to resonance between the incident light and surface plasmons. By increasing the rotational speed of an optical chopper used to measure the change in the output characteristics of the device, and comparing this with the simulated result, it is found that the constant charge produced by the piezoelectric effect arose due to the superposition of charge phases in the device.

Introduction

Humanity has continuously increased the use of fossil fuels since industrialization. The use of fossil fuels inevitably increases carbon emissions. Therefore, it is predicted that it will cause environmental pollution and climate change and have a serious impact on future generations. Thus, the energy problem has become a common task to be solved by all mankind, not a problem of one individual or one country. In order to develop a sustainable and clean energy source, many researchers are developing technologies such as nuclear fusion, hydrogen, wind, biomass, tidal power, geothermal, or seeking ways to reuse already used energy.[1–6] Reusing energy is called energy harvesting and is mainly suitable for small-scale energy sources. Light, heat, friction, vibration, and magnetic field are used as sources for energy harvesting and it is used as methods such as photovoltaic, thermoelectric, triboelectric, piezoelectric, and electromagnetic induction.[7–17] Among these, the piezoelectric method is a promising unconventional energy source that converts vibrations or pressure into electrical energy. Its advantages include high power density and wide applicability compared with other technologies. Suitable vibrations are commonplace: human motion, objects' vibrations, and sound waves can all provide energy, making piezoelectric generation in a potentially efficient, simple, and inexpensive way of powering various IoT devices.[18–20] However, some environments do not have the necessary movements or vibrations. An alternative energy source that can always be obtained in daily life is light. Solar cells represent the first technology that harvests electrical energy from the environment. However, they face the disadvantage of complicated manufacturing of solar cells, and the choice of materials is restricted to those with an energy band gap smaller than that of the light wavelength. An alternative way to harvest light energy uses radiation pressure to stimulate a piezoelectric material, whereby the pressure exerted on a surface is caused by the exchange of momentum between it and the photons of incident light. However, the radiation pressure of sunlight on Earth is too weak to be useful. This greatly limits the potential for light to generate electricity in a piezoelectric material, and amplification is necessary if light is to be used as the only energy source.

The interactions and correlations between metal structures and light have been studied with various purposes, including the development of optical tunable filters, extraordinary transmission, and optical amplification.[21–23] Research on the optical amplification has been studied to find out the relationship between metal structures and wavelength in devices.[24,25] These studies have used the principle that the light intensity increases as a result of the surface plasmon phenomenon. Surface plasmons (SPs) are a phenomenon in which electrons on the metal surface collectively vibrate at the boundary between a dielectric material and a conductive metal.[26] SPs can be classified as extended surface plasmons (ESPs) and localized surface plasmons (LSPs). They each form a strong electric field; however, when they overlap, they can create an ultrahigh local electric field near the metal surface. Because both ESPs and LSPs can be excited by incident light when nanostructures exist on the metal surface, we can expect a very strong electric field amplified by the superposition of LSPs and ESPs.[27,28]

We recently reported an innovative method for generating electrical energy using the light pressure.[29,30] The incident laser light on nano-sized Pt metal roughness inside the unique crater-like structure generated electricity by acting on lead zirconate titanate (PZT), a piezoelectric material. And we obtained an average current of 3.2 μA and a voltage of 200 mV by irradiating pulsed laser light of 401 nm wavelength and 11.1 mW power into the device named as light pressure electric generator (LPEG).[30] In addition, we could explain that the generated current and voltage are caused by the pressure of amplified light through the analysis of the output, obtained by using different piezoelectric materials (PZT, BNKT) in the same structure and the linear characteristics of the current according to the laser intensity. Furthermore, this paper was able to obtain optimized top electrode conditions using different noble metals under solar simulator (AM 1.5G). As a result, current, voltage, and power density of 3 μA, 250 mV, and 396 μW cm^{-2} were obtained when the top electrode was Ag 60 nm, respectively. And the direct current mechanism was explained using FDTD simulation and COMSOL Multiphysics analysis. The piezoelectric device developed in this study has a significant advantage in cost and efficiency because it can use the direct current generated from sunlight to charge a battery.

Results and discussion

Previously, we showed that a piezoelectric material PZT could be stimulated by increasing laser radiation pressure.[29,30] In this study, direct current was generated by amplifying the intensity of sunlight. The output principle and schematic diagram of the LPEG operated by solar radiation pressure (SRP) are shown in the Figure 1. The SRP reaching the surface of the Earth from the sun is ≈4.6 μPa, which is too weak to stimulate a piezoelectric material to generate a current. However, we expect that if the light (solar radiation) pressure can be sufficiently amplified using SPs in the LPEG operational region (i.e., the piezoelectric material region), the piezoelectric effect will generate a current. The SRP is amplified in the LPEG operational part inside the crater structure fabricated by wet-chemical etching of a GaAs (100) wafer. This is because the SRP generates a SP resonance resulting from the nano-scale roughness formed on the metal surface (i.e., top electrode) inside the crater with a unique structure. It has been reported that Raman scattering can be enhanced to a very large intensity because of the enhanced electric field resulting from the excitation of SP resonance, and we confirmed this by measuring the Raman spectrum.[31] The amplified SRP can deform the piezoelectric material to produce electricity. The technology developed here can use a wide wavelength range, including visible light, and is expected to be used for new energy harvesting technologies based on sunlight.

We fabricated a crater structure with both top and bottom openings, as shown in Figure 1 by etching a GaAs (100) wafer using a wet-chemical etching method.[32] After metal (Pt/Ti) deposition on the substrate on which the crater was formed, a PZT material having a Pb(Zr0.52,Ti0.48)O3 composition was used to coat the substrate by employing a sol–gel solution. The piezoelectric constant (d33) of PZT coated on the crater was ≈115 pC/N (Figure S1, Supporting Information). The LPEG comprises a top electrode/piezoelectric material/bottom electrode/wet-chemical etched GaAs (100) wafer (Figure 2a). We measured the LPEG image with a high-resolution optical 3D surface analyzer (Figure 2b), and confirmed from the field emission scanning electron microscope (FESEM) image that the bottom electrode, PZT, and top electrode were deposited sequentially (Figure 2c,d). However, the PZT thickness increases along the crater slope (Figure S2, Supporting Information) because gravity increases the PZT thickness toward the crater bottom during sol–gel coating. Therefore, we believe that nano-roughness is formed on the PZT and top electrode owing to the stress caused by this thickness difference (Figure 2e). At 700 Hz, the PZT thin film in the crater had a dielectric loss (tanδ) value of 0.036 (Figure S3, Supporting Information). Although PZT was coated inside the crater, we were able to obtain a high-quality PZT thin film. In addition, to confirm that the PZT in the crater can act as a piezoelectric material, Raman spectrum was obtained to characterize the PZT phases using a 532 nm laser line (Figure 2f). The Raman peaks, correspond to the E(2TO), ET+B1, A1(2TO), and A1(3LO) modes, agree well with the typical results for perovskite PZT.[33] The Raman spectrum shows that the PZT inside the crater has tetragonal phases, exhibiting outstanding piezoelectric properties. The incident sunlight excites SPs due to a roughness of several hundred nanometers or less that exists on the top electrode inside the crater, and the strong light pressure formed by the SPs stimulates the PZT to generate electrical energy.

To compare the amplification of light pressure for the various top electrode materials, Ag, Pt, Au, and Ni, which are transition metals known to form SPs in the visible light region, were deposited on the PZT layer by e-

beam evaporation. We measured the current and voltage characteristics generated by the LPEG under a solar simulator (AM 1.5G). Figure 3a shows short-circuit current, and Figure 3b shows open-circuit voltage generated by each device. For the LPEG with Ag-top electrode, the current and voltage were 500 nA and 112 mV, respectively, showing the largest output. For the Pt-top electrode, the outputs were 116 nA and 25 mV, for the Au-top electrode, 20 nA and 3 mV, and for the Ni-top electrode, 1.1 nA and 0.18 mV. That is, compared to the case of the Ni-top electrode, the current and voltage generated by a device with Ag-top electrode increased by ≈454% and ≈622% respectively.

When the PZT layer is irradiated by light, electrical output can be generated not only by the piezoelectric effect but also by the photovoltaic effect. To investigate the mechanism of the electrical output of the LPEG, we measured the output when AM 1.5G light passed through a long-pass filter (Edmund OD 2.0, long-pass filter). The long-pass filter does not transmit light shorter than 400 nm, but transmits more than 90% of light between 400 and 1000 nm. Compared to full AM 1.5G illumination, the output of the LPEG decreased by 0.91 times (inset of Figure 3a). The output produced by the LPEG is not due to the photovoltaic effect because light shorter than 400 nm, which corresponds to the energy gap of the PZT (3.53 eV), must be irradiated in order to produce a photocurrent due to the photovoltaic effect.[34] Figure 3a shows that the piezoelectric effect causes electrical output when light is irradiated on the LPEG, because the output of the LPEG is proportional to the total amount of light (i.e., light pressure) applied to the LPEG.

We focused on two phenomena in the measurement results shown in Figure 3a. First the output current and voltage vary depending on the top electrode materials; second when the sample is irradiated by sunlight, direct current is generated, not an alternating output. In order to help clarify the reason why the output of the LPEG differs depending on the type of metal, even with identical illumination, the LPEG was immersed in 0.1 M pyridine aqueous solution and the Raman spectrum was measured. Raman spectra were measured under the same conditions for all the samples (Figure S4, Supporting Information). Outside the crater without nano-scale surface roughness, the Raman intensity was similar and weak regardless of the top electrode metal (Figure S5, Supporting Information). However, for all top electrodes, the intensity of the pyridine Raman peaks significantly increased inside the crater. This indicates that the electric field was significantly enhanced by the SPs excited by the incident light inside the crater covered by the top electrode with nano-scale roughness (Figure S5, Supporting Information). Figure 3c shows the Raman measurements inside the crater. Regardless of the type of metal, the Raman peaks from the pyridine were observed near 1001 and 1031 cm−1. Unlike outside the crater, the Raman intensity inside the crater varies greatly depending on the top electrode materials. If the case of Ni is 1, the Raman intensity changes as Au: 1.06, Pt: 1.57, and Ag: 5.24 times, which is consistent with the current and voltage measurement results of the LPEG measured under AM 1.5G (Figure 3a,b).

We calculated the change in the electric field on the metal surface due to SPs using FDTD simulation when the crater structure was irradiated with 537 nm light. In all cases, a roughness of several hundred nanometers or less was formed on the metal surface inside the crater structure, and only metal types were changed to Ag, Pt, Au, and Ni. Figure 3d shows FDTD electric field intensity distributions for different metals, and Figure 3e shows a maximum square value of the electric field magnitude for each metal. According to FDTD simulation, the electric field was strongest for Ag, and the electric field strength gradually decreased in the order of Pt, Au, and Ni. Figure 3f shows that Ag has the highest light absorption and can excite SPs well; however, the resonance between the incident light and SPs gradually weakens in the order of Pt, Au, and Ni. That is, incident light excites the SPs the best on the Ag surface.

In general, COMSOL Multiphysics can be used to view the surface plasmon propagation of dielectric-metal-dielectric waveguides, but it is not easy to adjust the optimal conditions for SP propagation in a crater structure. Therefore, here, the COMSOL Multiphysics was used to determine the potential value corresponding to the electric field intensity, instead of revealing the excitation or propagation characteristics of the SPs. Therefore, the increased electric field was converted to the pressure using $P = (2/c^2\mu_0)|E_{max} \times \sin 2\pi ft|^2$. Then, the pressure was applied to COMSOL to obtain the electric potential distribution. Figure 3g–j shows that a larger potential is formed for the Ag top electrode compared to Pt, Au, and Ni top electrodes, which is in good agreement with the Raman spectra and FDTD simulation. From the Raman spectra, FDTD simulation, and COMSOL Multiphysics analysis, it can be seen that the amplification level of the electric field by the SPs varies depending onthe top electrode metal; the LPEG output is also consistent with these results.

We discuss the phenomenon in which a constant output current and voltage are generated by the piezoelectric

effect of the PZT when light irradiates a crater-structured LPEG. Figure 4a shows the FDTD simulation of the electric field with time when a light of 537 nm irradiates the crater structure with nanoroughness. Even if a constant intensity of continuous light irradiates the LPEG, the intensity of the light at each part of the crater slope is not constant. Figure 4b shows irregular light pressure being continuously applied to a point on the slope of the crater. In each part of the inclined surface of the crater, charge formation and discharge are independently generated by the piezoelectric effect of the PZT by incident light.[30] That is, similar amounts of charge are continuously and repeatedly generated and dissipated over time in the hot spots, where the light on the inner slope of the crater is amplified (Figure 4c; Figure S6, Supporting Information). At this time, the phase of the generated charge overlaps to maintain direct current based on Kirchhoff's law and the linear circuit superposition principle.[35] Constant charge formation by the SRP continuously acting on the metal surface with an irregular size was experimentally observed using a charge meter as follows. The charge peak and depolarizing charge were clearly visible when a 1-mW, 532-nm laser line was shone onto the device through an optical chopper when the chopper's revolutions per minute (rpm) were low. However, as the rpm increases, the gap between charge peaks is getting narrower and narrower. If the rpm is increased beyond the time resolution of the charge meter, that is, when a continuous laser is irradiated on the LPEG, a continuous charge is expected (Figure 4d). In addition, by composing the internal circuit in the COMSOL Multiphysics program, the charge of the LPEG was calculated as time-dependent. Although different values are shown for each top electrode material, it can be confirmed that they all converge to a constant value (Figure S7, Supporting Information).

We confirmed that the Ag-top electrode exhibited the largest electrical output and amplification of the Raman signal (Figure 3). The average thickness of the Ag top electrode (t_e) was 100 nm. The resonance between incident light and SPs is affected by the surface roughness; when the thickness of the metal electrode changes, the surface roughness also changes. Therefore, the change in the electrical output and Raman signal of the LPEG was measured while changing the average t_e from 20 to 100 nm. (Measurement processes in Figure S8, Supporting Information).

Load resistance was varied from 1–1000 kΩ, and output voltage and current were measured (Figure 5a,b). As load resistance increases, output voltage gradually increases and saturates, whereas the output current gradually decreases to saturation. The saturated values of the output voltage and current of the LPEG were maximum when t_e was 60 nm, and the output decreased in the order of 80, 40, 100, and 20 nm. To calculate the power density, we divided the square of V_{dc} into resistance ($P = V^2/R$, where P is the power, V_{dc} is the measured voltage, and R is the resistance). When t_e = 60 nm, a maximum peak power density (P_{max}) of ≈396.4 μW cm^{-2} was obtained at a resistance of 80 kΩ. P_{max} = ≈212.3 μW cm^{-2} at 70 kΩ for t_e = 80 nm, P_{max} = ≈70.8 μW cm_{-2} at 80 kΩ for t_e = 40 nm, P_{max} = ≈21.2 μW cm^{-2} at 400 kΩ for te = 100 nm, and P_{max} = ≈19.3 μW cm^{-2} at 200 kΩ for t_e = 20 nm (Figure 5c). When t_e = 60 nm, the output was increased ≈20.5 times compared to the case of t_e = 20 nm. Therefore, the t_e affects the output significantly.

To confirm the Ag top electrode thickness effect on crater roughness, we observed the inside of the crater using FE-SEM (Figure S9, Supporting Information), and the results are shown in Figure 5d. When t_e = 20 nm, Ag particle size distribution is generally 20–40 nm. And the particle size increases as t_e increases: the Ag particle size has a distribution of 30 to 60 nm for t_e = 40 nm, 50 to 80 nm for t_e = 60 nm, 60 to 100 nm for t_e = 80 nm, and 100 to 160 nm for t_e = 100 nm. It is considered that the maximum electrical output at t_e = 60 nm is the result of the best resonance between the incident visible light and SP under this surface condition, and Evanoff Jr et al. also reported that the Ag particle size distributed in 50–80 nm resonates best with visible light.[36] This shows the relationship between the surface roughness and the resonance wavelength. Because the intensity of the light is amplified by the SPs inside the crater, it confirms once again that the electrical output can be obtained from the LPEG even with a weak incident light pressure. To analyze the correlation between the particle size and amplification of incident light by SPs, we measured the Raman spectrum inside the crater and presented it as a 3D plot in Figure 5e. The Raman spectra measured outside the crater are shown in Figure S10 (Supporting Information). Unlike inside the crater, the intensity of the Raman peaks was hardly affected by Ag top electrode outside the crater. Because surface roughness is not formed outside the crater, amplification of incident light by SPs cannot be expected. The Raman peak intensity inside the crater was strongest when t_e was 60 nm (green line) and decreased as follows: 80 nm (blue), 40 nm (red), 100 nm (orange), and 20 nm (black) (Figure 5e). This is consistent with the output result for the LPEG shown in Figure 5c, and confirms the direct correlation between the magnitude of the surface roughness and the amplification of the incident light by SPs. The intensity of Raman spectrum of LPEG with t_e = 60 nm, showing the highest output, increased ≈54 times inside the crater compared

to outside (Figure S11, Supporting Information). This is because the crater structure and the roughness of inner surface achieved an optimal combination to significantly amplify the incident light.

Conclusion

We developed a piezoelectric energy-harvesting device that generates direct current under a solar simulator (AM 1.5G). The LPEG generated electrical output through the piezoelectric effect by greatly amplifying the intensity of incident light, using the nano-roughness of the top electrode combined with a unique crater structure. The dependence of the output of the device upon the type of LPEG top electrode was confirmed. Because the SRP inside the crater is amplified by the SPs excited by the incident light, electric energy from the piezoelectric effect can be obtained using the weak incident SRP. Amplification of SRP inside the crater was confirmed by Raman spectrum measurement, FDTD simulation, and COMSOL Multiphysics. In addition, it was shown that direct current can be output by the piezoelectric effect through the analysis of the change in electric field with time inside the crater for incident light of constant intensity using FDTD simulation. When the roughness of Ag top electrode was 50–80 nm, in which best resonance between the incident visible light and SP was expected, the maximum output power of ≈396 μW cm^{-2} was generated. Based on the results, we are willing to optimize the type and thickness of piezoelectric materials to further improve device output, and for operation in infrared or terahertz wavelength bands.

Experimental Section

Device Fabrication: The device fabrication process was as follows: i) A circular pattern with a diameter of 50 μm was formed on a GaAs (100) wafer capped with 300 nm thick SiO_2 using photolithography. The photoresist and SiO_2 layer were sequentially removed using acetone and a buffered oxide etchant, so that only the GaAs region corresponding to the crater was exposed. ii) The thickness of the wafer was adjusted to 100 μm by lapping to control the size of the crater. iii) The lapped wafer was pasted onto glass and etched in a solution of H_2SO_4:H_2O_2:H_2O = 1:5:5 for 2 h at room temperature to form a crater. iv) The bottom Pt/Ti electrode (100 nm/10 nm) was deposited by e-beam evaporation. v) A PZT layer was coated on the bottom electrode as follows: a commercial PZT solution of 0.4 mol was spin-coated at 3000 rpm for 45 s, followed by pyrolysis on a hot plate at 250 °C for 5 min and 300 °C for 3 min in air. The coating process for the PZT layer was repeated four times. The PZT layer underwent rapid thermal annealing at 650 °C for 5 min under a nitrogen atmosphere. vi) Finally, top electrodes of Ag, Pt, Au, and Ni were deposited on the PZT layer by e-beam evaporation. Details of device fabrication were referred to in a previous report.[29]

Measurements: A solar simulator (AM. 1.5G), and laser light with a wavelength of 532 nm were used as the incident light. The width of the laser pulses was controlled using an optical chopper, and the laser spot size on the LPEG was ≈7.9 × 10−7 m2. The electrical output of an LPEG was measured using two-probe method under laboratory conditions (temperature = 20–22 °C in ambient air). The current, voltage, and amount of accumulated charge were measured using a source meter (Tektronix, Cleveland, United States) and charge amplifier (Charge Amplifier 5015A, Kistler, Switzerland), respectively. The cross-sectional layer and surface of the top electrode were observed using a FESEM (CLARA, Tescan, Czech Republic). The overall shape of the crater, which constitutes the core of the device, was observed using a high-resolution 3D microscope (VHX-7000; Keyence, Japan). Raman spectra were obtained using a UniDRON Raman spectrometer (UniNanoTech, Yongin, Korea) equipped with a grating of 1200 grooves mm^{-1} in backscattering geometry under a laboratory environment. The 532 and 633 nm laser light was incident on the device through a 10 × /0.3 NA objective lens.

Computational Details: Commercial Lumerical FDTD software was used to simulate the tendency of an enhanced electric field on rough surfaces and the distribution of potentials in a 3D crater structure, depending on the type of metal. Perfectly matched layers that completely absorbed light without reflection were applied to the upper and lower layers of the FDTD region. A simulation time of 10000 fs was sufficient to observe the exact plasmon phenomenon. The electric field monitor was set to include part of the object. A total-field scattered-field source with a wavelength of 537 nm was propagated along the y-axis at the top of the object. The GaAs crater structure on which the light was incident in the simulation was modeled using 3D CAD (Autodesk, San Rafael, USA), and the materials of the structure were set as Ag, Pt, Au, and Ni using the built-in tool of the FDTD software. In the simulation, a surface with a random roughness of several tens of nanometers was used; the roughness was expressed by referring to the FESEM image of the Pt surface.

Commercial COMSOL Multiphysics software was used to simulate the tendency of the generated electric potential in the piezoelectric layer. A piezoelectric COMSOL simulation at a reduced scale was performed to confirm this tendency. For the simulation, the piezoelectric layer was Pb(Zr,Ti)O3-5H with a thickness of 500 nm.

Two transformation elements were required to simulate the piezoelectric effect. First, the elasticity matrix cE, a factor for calculating the applied stress as a mechanical strain, and then a coupling matrix eES for calculating the mechanical strain as the amount of charge generated by the piezoelectric effect, were applied. A top electrode (Ag, Pt, Au, and Ni) with a thickness of 100 nm was used as the top electrode, and Pt with a thickness of 100 nm and Ti with a thickness of 10 nm were used as the bottom electrode. The GaAs wafer was completely fixed assuming an ideal case. The force was amplified by applying an enhanced electric field perpendicular to the surface of the upper electrode. The force transmitted to the piezoelectric layer was calculated using the mechanical properties of Ag {Density 10490 [kg m^{-3}], Young's modulus 83 [GPa], Poisson's ratio [0.37]}, Pt {Density 21090 [kg m^{-3}], Young's modulus 168 [GPa], Poisson's ratio [0.38]}, Au {Density 19300 [kg m^{-3}], Young's modulus 78 [GPa], Poisson's ratio [0.44]}, and Ni {Density 8908 [kg m^{-3}], Young's modulus 200 [GPa], Poisson's ratio [0.31]}. The elasticity factor and piezoelectric coupling factor of Pb(Zr,Ti)O3-5H used are shown in Figure S12 (Supporting Information).

Supporting Information

Supporting Information is available from the Wiley Online Library or from the author.

Acknowledgements

This work was supported by the National Research Foundation of Korea (NRF) grant funded by the Korea government (MSIT) (no. 2022R1F1A1069919), and Korea Institute for Advancement of Technology (KIAT) grant funded by the Korea Government (MOTIE) (P0012451, The Competency Development Program for Industry Specialist).

Data Availability Statement

The data that support the findings of this study are available from the corresponding author upon reasonable request.

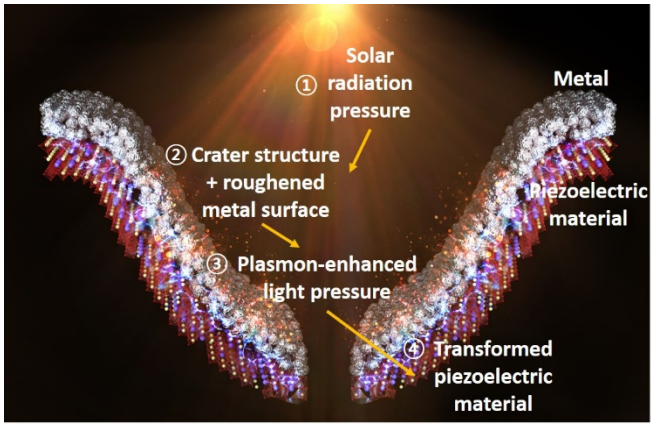

Fig. 1 | Concept of solar radiation pressure electric generation. Illustration of the proposed light pressure electric generating approach.

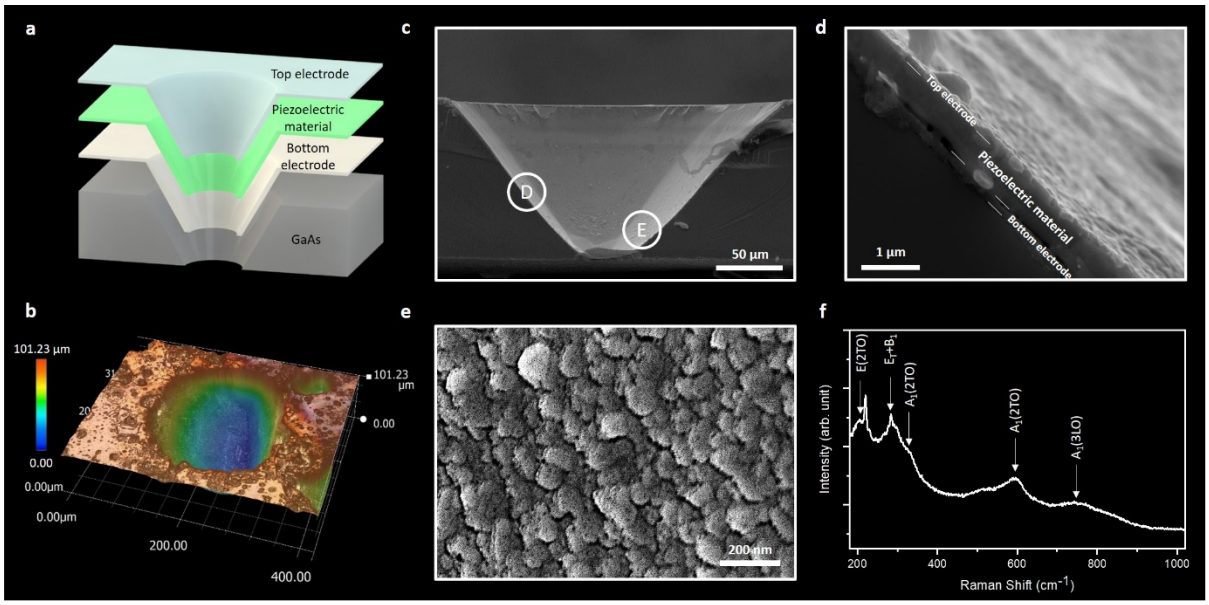

Fig. 2 | Structure of the LPEG. a-c, Cross-sectional schematic of the structure, high-resolution 3D optical image and cross-sectional FE-SEM of the sample. **d**,**e**, Cross-sectional FE-SEM image of point D and top view FE-SEM image of point E shown in c, respectively. **f**, Raman spectrum of the PZT layer inside the crater. The indexed sharp spectra agree well with that of typical perovskite-structured PZT.

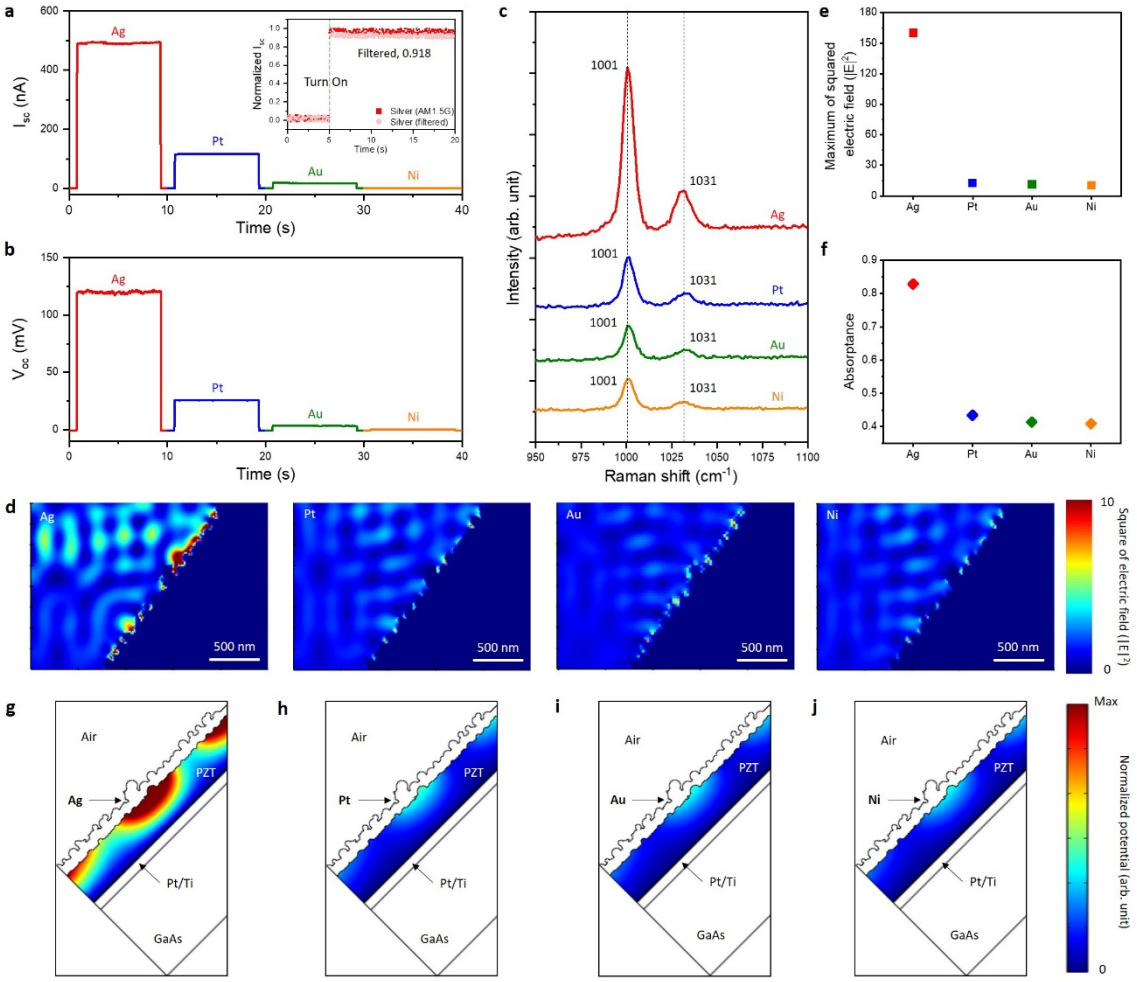

Fig. 3 | Electrical and optical characterization of LPEG with various electrodes. a,**b,** Output of short-circuit current and open-circuit voltage with various electrodes under AM 1.5G; inset: normalized short-circuit current curve of the Ag 100 nm sample measured under AM 1.5G and long-pass filtered illumination. **c**, Raman spectra inside the craters, coated with various metals, in an aqueous 0.1 M pyridine solution. **d-f**, Cross-sectional electric field intensity distributions, maximum electric field intensity graph and absorptance graph with various electrodes. **g-j**, COMSOL simulation of the electric potential distribution in the crater structure for Ag, Pt, Au, and Ni surface.

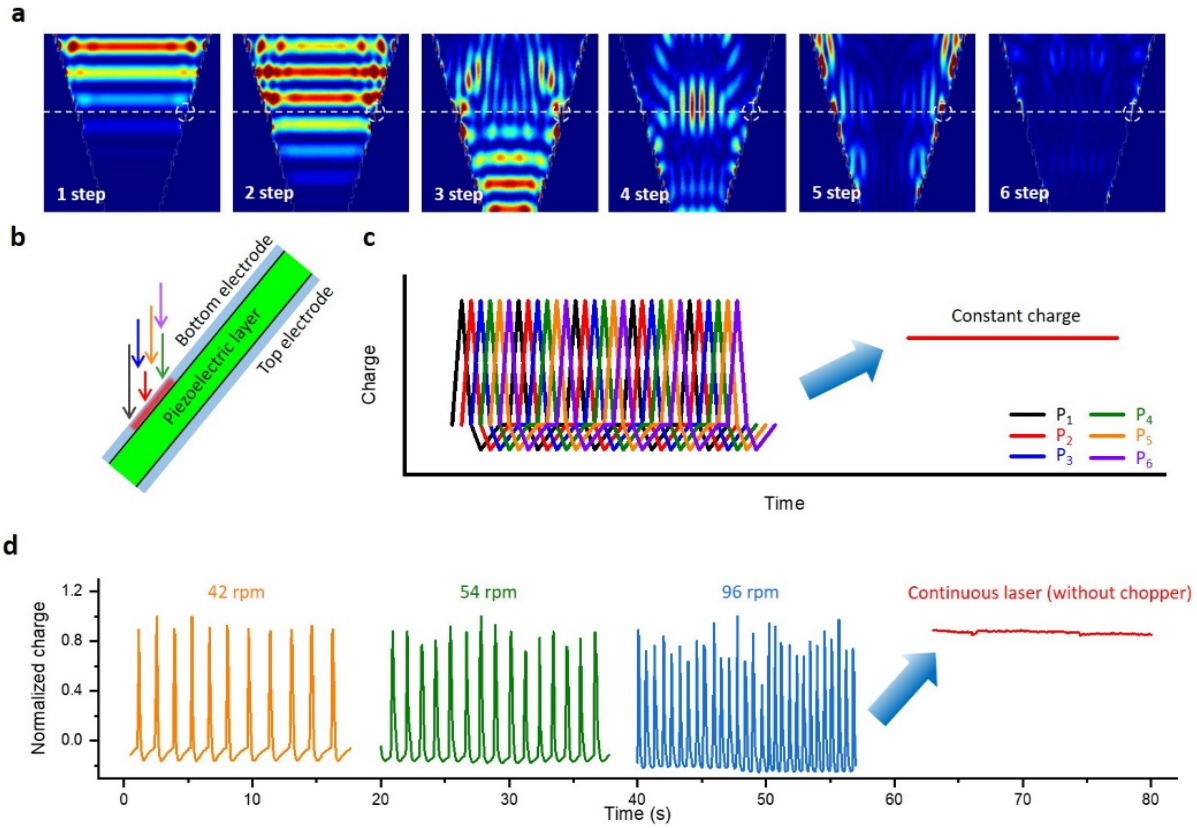

Fig. 4 | Mechanism for the constant electrical output in the LPEG device. a, Display of electric field changes in time monitor video of FDTD simulation divided by regular time intervals. **b**, Schematic diagram in which irregular pressure is continuously applied in one area. **c**, Schematic diagrams of the superposition of charge based on the phase-shift signal. **d**, Charges measured by increasing chopper rpm using a 532 nm laser.

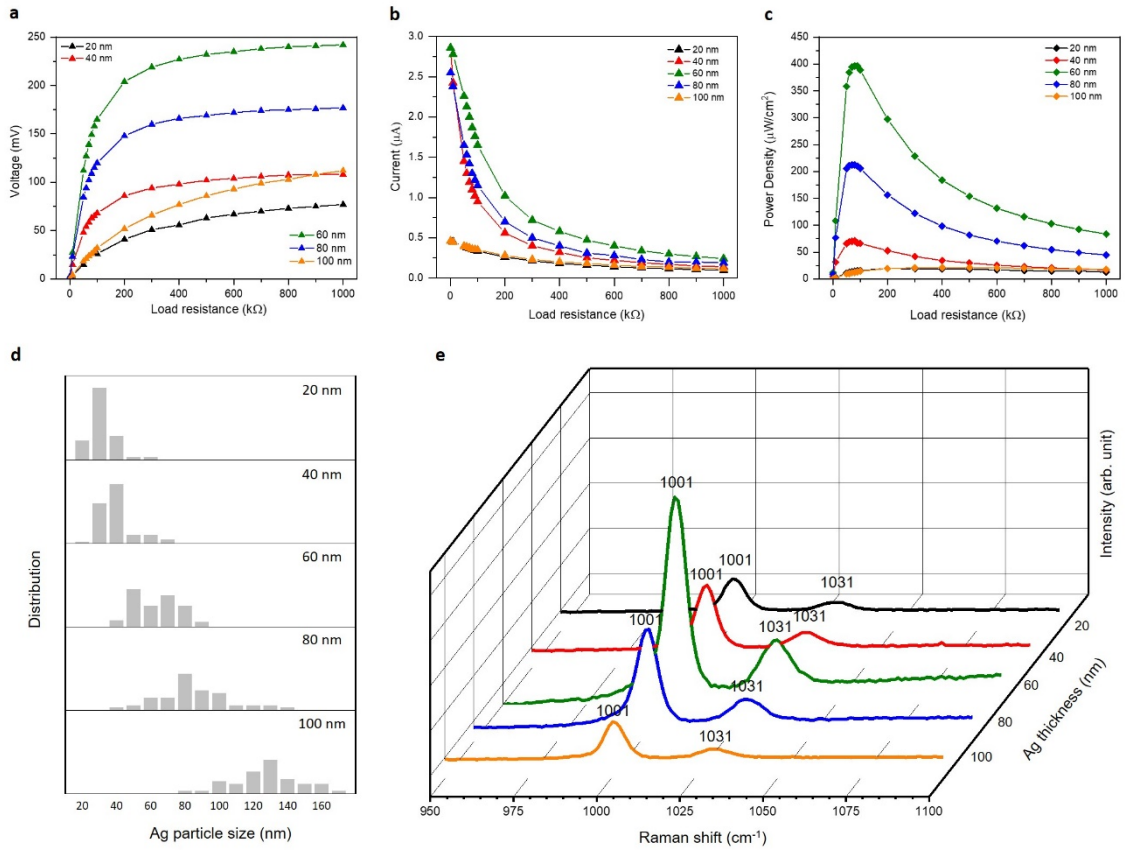

Fig. 5 | Electrical and optical characterization of LPEG with different Ag electrodes thickness. a-c, Measured output (a) DC voltage, (b) DC current, and (c) calculated power density under different load resistance varying from 1 kΩ to 1000 kΩ for LPEG with various Ag electrode thicknesses. **d**, Ag particle size distribution at various Ag electrode thicknesses. **e**, 3D plot of Raman spectra recorded at various Ag electrode thicknesses.

References

[1] A. F. Rowcliffe, C. E. Kessel, Y. Katoh, L. M. Garrison, L. Tan, Y. Yamamoto, F. W. Wiffen, Nucl. Mater. Energy 2018, 16, 82.
[2] M. Xie, S. Dunn, E. L. Boulbar, C. R. Bowen, Int. J. Hydrogen Energy 2017, 42, 23437.
[3] A. Truitt, S. N. Mahmoodi, Int. J. Precis. Eng 2013, 14, 1667.
[4] D. Abbas, D. Current, M. Phillips, R. Rossman, H. Hoganson, K. N. Brooks, Biomass Bioenergy 2011, 35, 4538.
[5] A. Sentchev, J. Thiebot, A.-C. Bennis, M. Piggott, Philos. Trans. R. Soc., A 2020, 378, 20190490.
[6] A. K. Tiwari, A. Kumar, P. Basu, Appl. Therm. Eng. 2022, 200, 117673.
[7] B. P. Lechene, M. Cowell, A. Pierre, J. W. Evans, P. K. Wright, A. C. Arias, Nano Energy 2016, 26, 631.
[8] A. Nozariasbmarz, R. A. Kishore, B. Poudel, U. Saparamadu, W. Li, R. Cruz, S. Priya, ACS Appl. Mater. Interfaces 2019, 11, 40107.
[9] K.-W. Lim, M. Peddigari, C. H. Park, H. Y. Lee, Y. Min, J.-W. Kim, C.-W. Ahn, J.-J. Choi, B.-D. Hahn, J.-H. Choi, D.-S. Park, J.-K. Hong, J.-T. Yeom, W.-H. Yoon, J. Ryu, S. N. Yi, G.-T. Hwang, Energy Environ. Sci. 2019, 12, 666.
[10] L. Zuo, X. Tang, J. Intell. Mater. Syst. Struct. 2013, 24, 1405.
[11] V. Annapureddy, H. Y. Lee, W.-H. Yoon, H.-J. Woo, J.-H. Lee, H. Palneedi, H.-J. Kim, J.-J. Choi, D.-Y. Jeong, S. N. Yi, J. Ryu, Appl. Phys. Lett. 2016, 109, 093901.
[12] S. Aftab, H. M. S. Ajmal, E. Elahi, H. M. M. U. Haque, S. M. W. Iqbal, J. Aziz, S. Yousuf, M. Z. Iqbal, M. A. Shehzad, ACS Appl. Nano Mater.. 2022, 5, 6455.
[13] S. Aftab, M. Z. Iqbal, Z. Haider, M. W. Iqbal, G. Nazir, M. A. Shehzad, Adv. Opt. Mater. 2022, 10, 2201288. [14] M.-J. Lee, J.-H. Ahn, J. H. Sung, H. Heo, S. G. Jeon, W. Lee, J. Y. Song, K.-H. Hong, B. Choi, S.-H. Lee, M.-H. Jo, Nat. Commun. 2016, 7, 12011.
[15] M. S. Kwak, K.-W. Lim, H. Y. Lee, M. Peddigari, J. Jang, C. K. Jeong, J. Ryu, W.-H. Yoon, S. N. Yi, G.-T. Hwang, Nanoscale 2021, 13, 8418.
[16] J. Ryu, J.-E. Kang, Y. Zhou, S.-Y. Choi, W.-H. Yoon, D.-S. Park, J.-J. Choi, B.-D. Hahn, C.-W. Ahn, J.-W. Kim, Y.-D. Kim, S. Priya, S. Y. Lee, S. Jeong, D.-Y. Jeong, Energy Environ. Sci. 2015, 8, 2402.
[17] M. S. Kwak, M. Peddigari, H. Y. Lee, Y. Min, K.-I. Park, J.-H. Kim, W.-H. Yoon, J. Ryu, S. N. Yi, J. Jang, G.-T. Hwang, Adv. Funct. Mater. 2022, 32, 2112028.
[18] C. Dagdeviren, B. D. Yang, Y. Su, P. L. Tran, P. Joe, E. Anderson, J. Xia, V. Doraiswamy, B. Dehdashti, X. Feng, B. Lu, R. Poston, Z. Khalpey, R. Ghaffari, Y. Huang, M. J. Slepian, J. A. Rogers, Proc. Natl. Acad. Sci. 2014, 111, 1927.
[19] H.-B. Fang, J.-Q. Liu, Z.-Y. Xu, L. Dong, L. Wang, D. Chen, B.-C. Cai, Y. Liu, Microelectron. J. 2006, 37, 1280.
[20] S. N. Cha, J.-S. Seo, S. M. Kim, H. J. Kim, Y. J. Park, S.-W. Kim, J. M. Kim, Adv. Mater. 2010, 22, 4726.
[21] C. Genet, T. W. Ebbesen, Nature 2007, 445, 39.
[22] D. B. Shao, S. C. Chen, Appl. Phys. Lett. 2005, 86, 253107.
[23] M. A. Seo, H. R. Park, S. M. Koo, D. J. Park, J. H. Kang, O. K. Suwal, S. S. Choi, P. C. M. Planken, G. S. Park, N. K. Park, Q. H. Park, D. S. Kim, Nat. Photonics 2009, 3, 152.
[24] M. L. Juan, M. Righini, R. Quidant, Nat. Photonics 2011, 5, 349.
[25] J. A. Schuller, T. Taubner, M. L. Brongersma, Nat. Photonics 2009, 3, 658.
[26] M. Z. Alam, Z. Yang, M. Sheik-Bahae, J. S. Aitchison, M. Mojahedi, Sci. Rep. 2021, 11, 3170.
[27] M. Abutoama, S. Li, I. Abdulhalim, J. Phys. Chem. C 2017, 121, 27612.

[28] M. Abutoama, S. Isaacs, M. Ney, L. Zhong, D. Li, L. Jiang, I. Abdulhalim, J. Phys. Chem. C 2019, 123, 12984.
[29] H. Y. Lee, M. S. Kwak, G.-T. Hwang, H. S. Ahn, D. H. Ha, S. N. Yi, Appl. Surf. Sci. 2022, 596, 153588.
[30] H. Y. Lee, M. S. Kwak, K.-W. Lim, H. S. Ahn, G.-T. Hwang, D. H. Ha, R. A. Taylor, S. N. Yi, Opt. Express 2021, 29, 35161.
[31] L.-W. Nien, S.-C. Lin, B.-K. Chao, M.-J. Chen, J.-H. Li, C.-H. Hsueh, J. Phys. Chem. C 2013, 117, 25004.
[32] H. Y. Lee, M. S. Kwak, K.-W. Lim, H. S. Ahn, S. N. Yi, Han'guk Chaelyo Hakhoechi 2019, 29, 115.
[33] K.-I. Park, C. K. Jeong, J. Ryu, G.-T. Hwang, K. J. Lee, Adv. Energy Mater. 2013, 3, 1539.
[34] S. Samanta, V. Sankaranarayanan, K. Sethupathi, Vacuum 2018, 156, 456.
[35] X. Li, C. Zhang, Y. Gao, Z. Zhao, Y. Hu, O. Yang, L. Liu, L. Zhou, J. Wang, Z. L. Wang, Energy Environ. Sci. 2022, 15, 1334.
[36] D. D. Evanoff, G. Chumanov, ChemPhysChem 2005, 6, 1221.

Author contributions

H. Y. Lee fabricated the LPEG device and performed the charge meter, solar simulator, FE-SEM measurements, high-resolution 3D optical microscope measurements, and FDTD simulation. H. Y. Lee, M. S. Kwak, and G. –T. Hwang performed source meter measurements. H. Y. Lee and D. H. Ha performed Raman measurements and analysed data. D. H. Ha and S. N. Yi analysed the current, voltage and charge data. S. N. Yi supervised this project. H. S. Ahn, D. H. Ha, R. A. Taylor, and S. N. Yi contributed to data interpretation. H. Y. Lee, D. H. Ha, R. A. Taylor, and S. N. Yi contributed to the writing of the manuscript. All the authors discussed the results and commented on the manuscript.

Correspondence and requests for materials should be addressed to D.H.H and S.N.Y.

*e-mail: snyi@kmou.ac.kr
*e-mail: dhha@kriss.re.kr

[1]Interdisciplinary Major of Maritime AI Convergence, Korea Maritime & Ocean University, Busan 49112, Korea
[2]Major of Nano-Semiconductor Engineering, Korea Maritime & Ocean University, Busan 49112, Korea
[3]Department of Materials Science and Engineering, Pukyong National University, Busan 48513, Korea
[4]Department of Physics, University of Oxford, Parks Road, Oxford OXI 3PU, United Kingdom
[5]Materials and Convergence Measurement Institute, Korea Research Institute of Standards and Science, Daejeon, 34113, Korea